

Supporting Information:

Robust and accurate electric field sensing with solid state spin ensembles

Julia Michl,^{*,†} Jakob Steiner,[†] Andrej Denisenko,[†] André Bülau,[‡] André Zimmermann,[¶] Kazuo Nakamura,[§] Hitoshi Sumiya,^{||} Shinobu Onoda,[⊥] Philipp Neumann,^{*,†} Junichi Isoya,[#] and Jörg Wrachtrup[†]

[†]*3. Physikalisches Institut, University of Stuttgart, Pfaffenwaldring 57, 70569 Stuttgart, Germany*

[‡]*Hahn-Schickard, Allmandring 9b, 70569 Stuttgart, Germany*

[¶]*Institut für Mikrointegration, University of Stuttgart, Allmandring 9b, 70569 Stuttgart, Germany*

[§]*Application Technology Research Institute, Tokyo Gas Company, Ltd., Yokohama, 230-0045 Japan*

^{||}*Advanced Materials Laboratory, Sumitomo Electric Industries, Ltd., Itami, 664-0016 Japan*

[⊥]*Takasaki Advanced Radiation Research Institute, National Institutes for Quantum and Radiological Science and Technology, Takasaki, 370-1292, Japan*

[#]*Faculty of Pure and Applied Sciences, University of Tsukuba, Tsukuba, 305-8573 Japan*

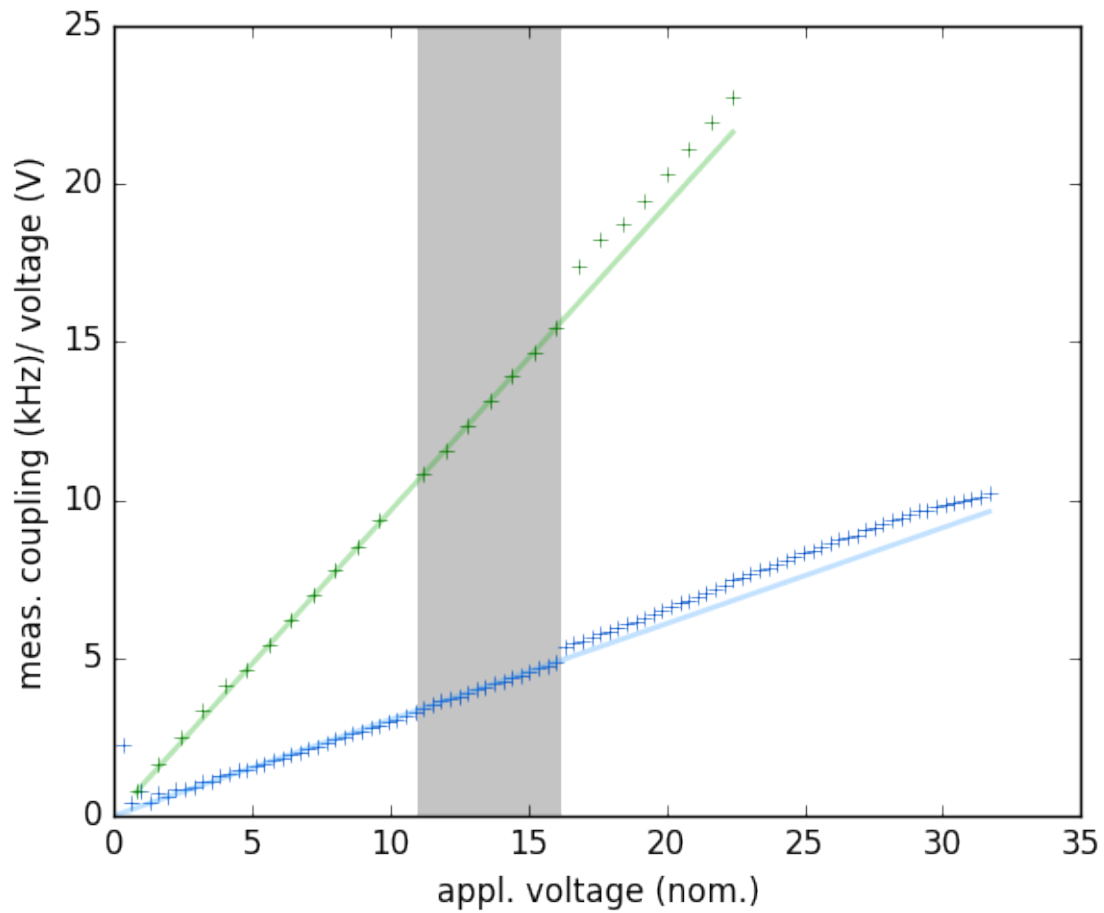


Figure S1: Fit of lines through origin for measured voltage over nominally applied voltage (green) for measurement with an oscilloscope and measurement of coupling to the NVs (blue). The grey area gives the part of data which was used for the fit.

Calculation of the coupling constant R_{2E}

For the application of an AC voltage signal to the plate capacitor, a Rigol AWG DG1022 was used. The signal from the signal generator was then amplified via an Op-Amp (LT1633CS) with a slew rate of 45 V/ μ s. For this setup, the actually applied voltage V_r is not equal to the nominally applied voltage V_n and this relation was measured via a Rigol DS1102E oscilloscope as seen in fig. S1. The factor between V_r and V_n of $p_1 = 0.966$ and the factor $p_2 = 0.3045$ kHz/V for the relation between V_n and frequency shift f_n of the NVs gives the desired factor c_m between V_r and f_r , using the following relations:

$$p_1 = \frac{\Delta V_r}{\Delta V_n}, \quad p_2 = \frac{\Delta f_n}{\Delta V_n} \quad (\text{S1})$$

and thus

$$c_m = \frac{\Delta f_r}{\Delta V_r} = \frac{p_2}{p_1} = 0.315 \text{ kHz/V}. \quad (\text{S2})$$

This gives the relation between the frequency shift of the NVs and the voltage applied to the structure. To get the desired coupling constant R_{2E} , the distance between the capacitor plates d has to be known, as the electric field is

$$E = \frac{V_r}{d}. \quad (\text{S3})$$

The coupling constant R_{2E} is also dependent on the angle of the transversal magnetic field ϕ_B as well as on the residual longitudinal magnetic field B_z , leading to a reduction of the frequency shift by a factor c_z , which can be calculated numerically from the measured magnetic field. Thus, the measured shift is given by^{S1}

$$\Delta f_r = R_{2E} \cdot \Delta E \cdot c_z \cos(2\phi_B + \phi_E) \quad (\text{S4})$$

and therefore the coupling constant is given by

$$R_{2E} = \frac{\Delta f_r \cdot d}{c_z \cdot \cos(2\phi_B + \phi_E)}, \quad (\text{S5})$$

where ϕ_E is the angle of the E-field within the xy-plane. With the values for ϕ_B , ϕ_E and c_z , calculated from the measurement of a full ODMR spectrum, gives the coupling constant as

$$R_{2E} = \frac{d \cdot 0.315 \text{ kHz/V}}{0.9614 \cdot 0.9874} \approx 165 \text{ kHz/V}/\mu\text{m}. \quad (\text{S6})$$

The determined coupling constant is within the margin of error of the coupling constant $R_{2E} = 175 \pm 30 \text{ kHz/V}/\mu\text{m}$ given by Van Oort.^{S2}

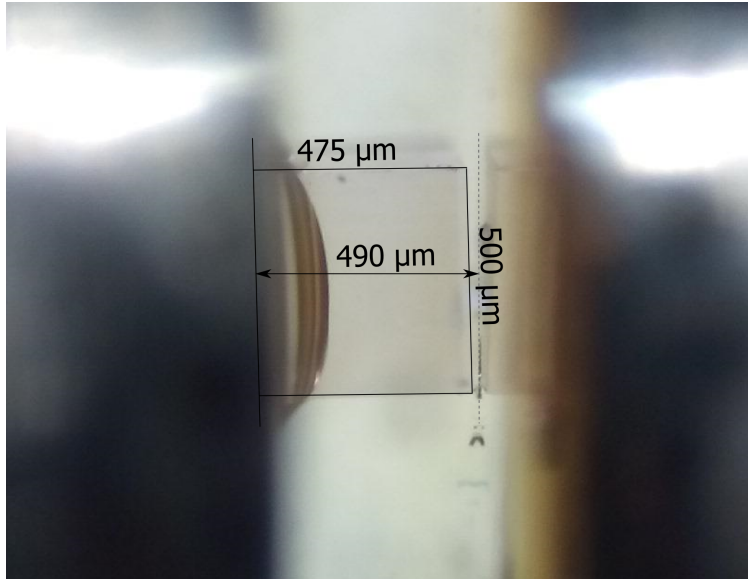


Figure S2: Diamond within plate capacitor. The dimensions of the diamond are known, thus the distance between the capacitor plates can be determined as $d = 490 \pm 20 \mu\text{m}$.

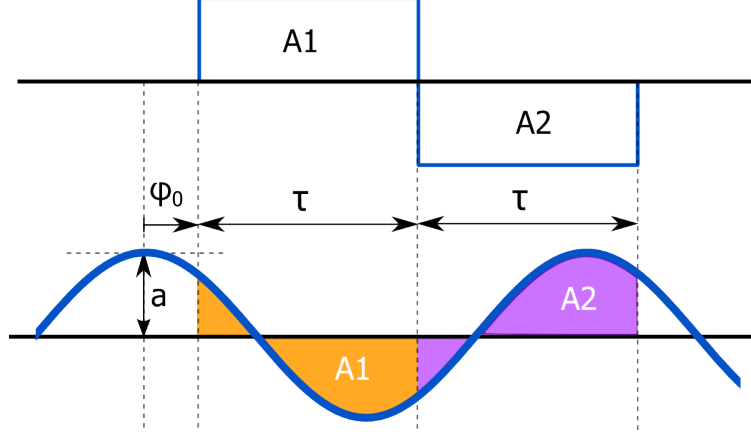


Figure S3: NV filter function and accumulated phase depending on the starting phase ϕ_0 .

Calculation of the amplitudes measured via a Qdyne-measurement

Collected Phase

For the accumulated phase Φ in dependence of the starting phase ϕ_0 of a sinusoidal signal we take

$$\Phi = A_1 - A_2 \quad (\text{S7})$$

$$= \int_0^\tau 2\pi a \cos(\phi_0 + 2\pi ft) dt - \int_\tau^{2\tau} 2\pi a \cos(\phi_0 + 2\pi ft) dt \quad (\text{S8})$$

$$= 2\pi a \left(- \left[\frac{1}{2\pi f} \sin(\phi_0 + 2\pi ft) \right]_0^\tau + \left[\frac{1}{2\pi f} \sin(\phi_0 + 2\pi ft) \right]_\tau^{2\tau} \right) \quad (\text{S9})$$

$$= \frac{2\pi a}{2\pi f} (\sin(\phi_0 + 2\pi f\tau) - \sin(\phi_0) + \sin(\phi_0 + 2\pi f\tau) - \sin(\phi_0 + 4\pi f\tau)) \quad (\text{S10})$$

$$= \frac{a}{f} (2 \sin(2\pi f\tau + \phi_0) - \sin(4\pi f\tau + \phi_0) - \sin(\phi_0)). \quad (\text{S11})$$

Here, f is the signal frequency, which is known. a is the amplitude of the coupling between NV and field in units of frequency. The 2π factor is necessary, as we need to integrate over an angular frequency to get a phase. The time τ is here the time between a $\pi/2$ and the

π -pulse of the Hahn-Echo measurement and is aligned to the signal frequency f by

$$\tau = \frac{1}{2f}. \quad (\text{S12})$$

This relation can now be used to further calculate eq. S11:

$$\Phi = \frac{a}{f} (2 \sin(\pi + \phi_0) - \sin(2\pi + \phi_0) - \sin(\phi_0)) \quad (\text{S13})$$

$$= \frac{2a}{f} (\sin(\phi_0 + \pi) - \sin(\phi_0)) \quad (\text{S14})$$

$$= -\frac{4a}{f} \sin(\phi_0). \quad (\text{S15})$$

This gives the phase collected by the NV superposition state within one Hahn-Echo measurement in dependence of the starting phase of the signal. As the phase of the NV is transferred onto the spin state populations using a final $\pi/2$ -pulse with the same phase as the first $\pi/2$ -pulse, the cosine of the collected phase is measured as the signal s :

$$s = \cos\left(\frac{4a}{f} \sin(\phi_0)\right). \quad (\text{S16})$$

Bessel function representation

Eq. S16 can be rewritten using Bessel functions, as given in the following relation:

$$\cos(\beta \sin(\theta)) = J_0(\beta) + 2 \sum_{n=1}^{\infty} J_{2n}(\beta) \cos(2n\theta). \quad (\text{S17})$$

Transforming eq. S16 using eq. S17 leads to

$$s = J_0\left(\frac{4a}{f}\right) + 2 \sum_{n=1}^{\infty} J_{2n}\left(\frac{4a}{f}\right) \cos(2n\phi_0). \quad (\text{S18})$$

The starting phase of the Hahn-Echo measurement is shifted between measurements by a fixed time difference δt , added to each measurement sequence. The length of the measure-

ment sequence itself is chosen as a multiple of the signal period, so that we can simply, for the sake of this calculation, set it to zero. This is justifiable as long as the signal coherence time far exceeds the total measurement time. Thus, the starting phase for the i -th measurement is given by

$$\phi_{0,i} = 2\pi f i \Delta t. \quad (\text{S19})$$

So, it can be seen as continuous with Δt as the distance between measurement points, meaning $\phi(i) \rightarrow \phi(t)$ with $t(i) = i\Delta t$. The signal then is

$$s(t) = J_0\left(\frac{4a}{f}\right) + 2 \sum_{n=1}^{\infty} J_{2n}\left(\frac{4a}{f}\right) \cos(4\pi n f t), \quad (\text{S20})$$

which is a Fourier series for the frequency $2f$, giving the amplitudes of the different orders n through the Bessel functions. The DC term, $J_0(4a/f)$ can be neglected here, as the DC component carries the most noise in nearly all measurements. For the true measurement signal, the contrast c , the difference between the dark and bright state, has to be taken into account, yet, this contrast can change significantly with changes in the laser power, or slight detunings for the microwave pulses. Therefore, an alternative figure of merit is the ratio between the amplitudes at different frequencies, as this ratio will only depend on the Bessel functions J_{2n} and is independent of contrast, number of measurement points and similar parameters.

Measurement of small signals

For this work, the measurement of the cosine of the accumulated phase is necessary, as the sign of the frequency shift is reversed for half the NVs, making the measurement of the sine of the phase impossible. Yet, if this were not the case, it would be possible to measure smaller signals, as $\cos \Phi \approx 1$ but $\sin \Phi \approx \Phi$ for small phases. In the Hahn-Echo measurement, this can be achieved via a 90° phase-shifted last $\pi/2$ -pulse. This sine function can be represented

using Bessel functions as

$$\sin(\beta \sin(\theta)) = 2 \sum_{n=0}^{\infty} J_{2n+1}(\beta) \sin((2n+1)\theta). \quad (\text{S21})$$

The Bessel functions in series representation are as follows:

$$J_n(\beta) = \frac{\beta^n}{2^n \Gamma(n+1)} \left(1 - \frac{\beta^2}{2(2n+2)} + \frac{\beta^4}{8(2n+2)(2n+4)} - \dots \right), \quad (\text{S22})$$

leaving J_1 as the only relevant Bessel function in eq. S21 for small β , as all others are at least $\mathcal{O}(\beta^2)$. In first order, for small β , J_1 also goes linearly with β :

$$2J_1(\beta) \approx 2 \frac{\beta}{2 \cdot \Gamma(2)} = \beta, \quad (\text{S23})$$

leading to the whole eq. S21 being reduced to

$$\sin(\beta \sin(\theta)) = \beta \sin(\theta), \quad (\text{S24})$$

which is the simple approximation $\sin x \approx x$ for small angles. So, for very small signals, measured through a sine, the amplitude of the signal will be proportional to the signal amplitude and the coupling.

Electric field measurements

As previously defined, a is the amplitude of the coupling between NV and field in units of frequency, so in the case of a transversal electric field signal $a = k_{\perp} \cdot E_{\perp}$, where k_{\perp} is the coupling constant. If a transversal magnetic field is used, a factor $\cos(2\phi_B + \phi_E)$, dependent on the electric field angle ϕ_E and the magnetic field angle ϕ_B , has to be taken into account for the coupling strength. If the applied field is also not perfectly aligned, the coupling strength is also reduced by a factor c_z , depending on the magnetic field B_z along the NV

axis. Taking everything into account, we are left for the amplitudes A_n of the different orders n of frequencies occurring in the measurement as

$$A_n = c_{\text{misc}} J_{2n} (4c_z \cos (2\phi_B + \phi_E) k_{\perp} E_{\perp}) / f. \quad (\text{S25})$$

The factor c_{misc} entails all components effecting the measurement contrast and also measurement effects which effect all frequency components equally, e.g. the factor 2 in eq. S20.

E-Field and B-Field inhomogeneities

By measuring on an NV-ensemble, there are always field gradients over the sample volume, leading to different NVs seeing slightly different fields. To calculate the effect of field inhomogeneities on the qdyne measurements presented in this paper, a gaussian field distribution where the width is assumed to scale linearly with the field strength. This leads to the signal from an ensemble

$$s = e^{-\frac{\Phi}{2\sigma}} \cos \Phi \quad (\text{S26})$$

and by substituting the accumulated phase as in eq. S16, the signal is

$$s = e^{-\left(\frac{c \sin \phi}{2\sigma}\right)} \cos (c \sin \phi) \quad (\text{S27})$$

and with a series expansion up to second order of the exponential function:

$$s = \left(1 - \frac{c^2 \sin^2 (\phi)}{4\sigma^2}\right) \sum J_{2n} (c) \cos 2\phi \quad (\text{S28})$$

and, using $\sin^2 x = (1 - \cos(2x))/2$:

$$s = s_0 - \sum \left(\frac{c^2}{8\sigma^2} J_{2n}(c) \cos (2n\phi) + \frac{1}{2} \cos (2\phi (n - 1)) + \frac{1}{2} \cos (2\phi (n + 1)) \right) \quad (\text{S29})$$

$$= \sum J_{2n}(c) + \frac{c^2}{16\sigma^2} (J_{2(n+1)} + J_{2(n-1)} - 2J_{2n}), \quad (\text{S30})$$

s_0 being the signal from a homogeneous field. In comparison to the measurement signal in homogeneous fields as shown in eq. 20, it can be seen here that inhomogeneous fields lead to a mixing of neighboring Fourier components.

Samples and structures

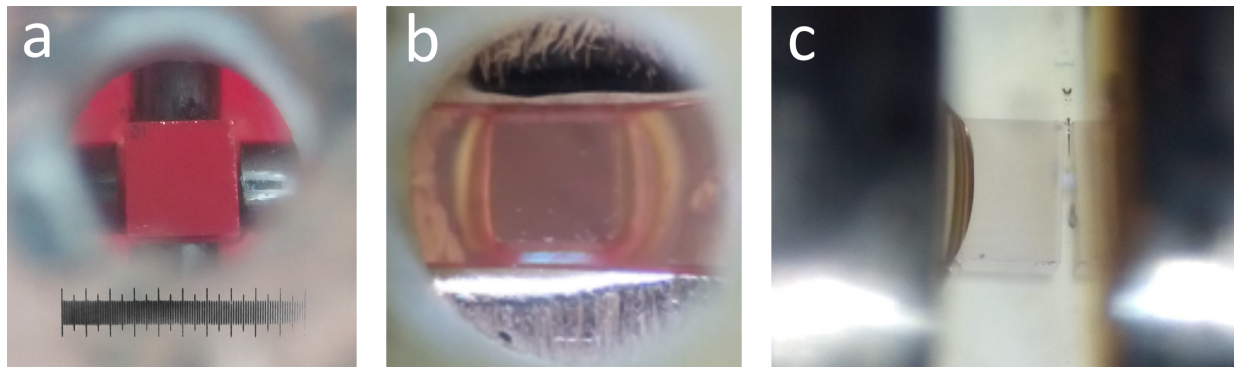


Figure S4: Used capacitor structures. (a) Four brass rods of 0.4 mm diameter can be used to rotate the electric field. The field from the rods is inhomogeneous and thus not well defined, but it was still possible to measure the direction dependence. The diamond is glued to a parabolic lens. (b) Two brass slabs of 500 μm height and 3 mm width. The diamond is again glued to a parabolic lens. The field is much more homogeneous than in the previous case, yet the limitation of the capacitor in one dimension to the height of the diamond makes the field weaker than expected for a plate capacitor. (c) Two brass rods with approx. 3 mm diameter. This structure allows for a well-defined field, as the capacitor plates are much larger than the sample volume at which the field is measured. It is also sufficiently close to an infinite plate capacitor, making it possible to use $E = V/d$ for the electric field. The diamond can not be glued to a lens, as in the cases before, thus the fluorescence detection has to be done via an air objective with a high working distance, limiting the achievable precision.

For all measurements presented here, two diamond cubes with $\approx 500 \mu\text{m}$ edge lengths were used. Both stones were cut from the same diamond and exhibit the same characteristics such as density of NVs and coherence times of NVs. One of those stones was etched on the four non-111 surfaces, to eliminate any effects from a possible graphite surface layer. We conducted electric field measurements using both samples and observed no difference. For the application of an electric field, three different capacitor structures were used, which are

shown in fig. S4. The first structure consists of four rods with a diameter of 400 μm , slightly below the side length of the diamond cubes. With this structure, the measurement of the angular dependence of the Stark shift could be verified for an ensemble of NVs. The high inhomogeneity of the field, especially a large distribution of the direction of the field, leads to the angle dependence being slightly averaged out. The measured shift over the applied electric field angle is shown in fig. S5. The second structure, fig. S4(b), consists of two brass slabs, which are as thin as the diamond sample, 500 μm . This allows for the diamond being glued to a parabolic lens, resulting in a high collection efficiency. So, this structure can be used for high precision measurement, even though the electric field from the electrodes do not make a homogeneous field, as they are very limited in one dimension. The third structure consists of two brass rods with a diameter of 3 mm. This allows for a well-defined electric field over the sample volume in the center of the structure. This structure was used for the measurement of the coupling constant R_{2E} , as described in the first section. As the capacitor is larger than the sample, the collection cannot be done with a parabolic lens and has to be done over an air objective with a large working distance. For this, an objective Mitotoyo M Plan Apo 100x Infinity Corrected Long WD objective was used.

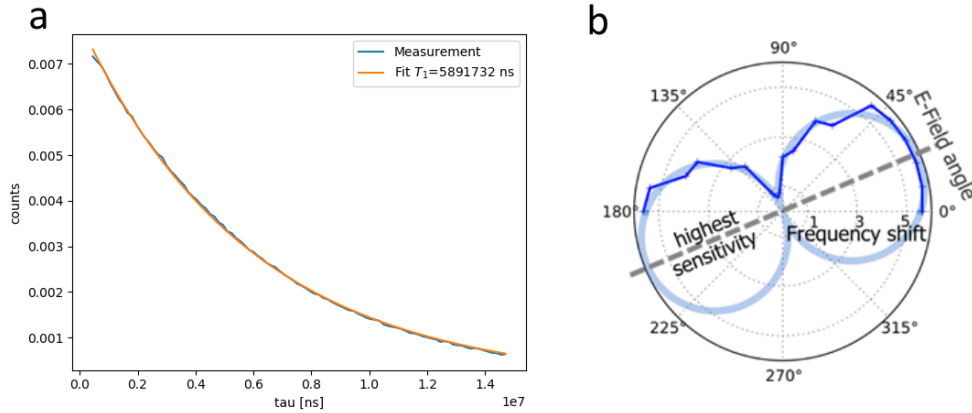


Figure S5: (a) T_1 measurement. The longitudinal coherence time is $T_1 \approx 6$ ms, measured via the difference of the fluorescence of the NV ensemble after time τ with and without a π -pulse, thus eliminating effects of charge state. (b) Angular dependence of shift caused by an electric field in kHz. The shift does not go to zero at $2\phi_B + \phi_E = \pi/2$, as the electric field does not have the same angle for all NVs.

Measurement of R_{15}

The complete Stark-shift Hamiltonian for the NV is determined by the C_{3V} symmetry and is given as

$$\begin{aligned} \hat{H}_{\text{Stark}} = & R_{15} (E_x (S_x S_z + S_z S_x) + E_y (S_y S_z + S_z S_y)) \\ & - R_{2E} (E_x (S_x^2 - S_y^2) + E_y (S_x S_y + S_y S_x)) \\ & + R_{3D} E_z \left(S_z^2 - \frac{1}{3} S(S+1) \right). \end{aligned} \quad (\text{S31})$$

Here, R_{2E} is the coupling constant to transversal electric fields, as discussed in previous chapters. The coupling constant to axial electric fields, R_{3D} , could not be measured during our experiments, as it is assumed to be 50 times smaller than the coupling constant R_{2E} . The remaining term of the Hamiltonian leads to a mix between the states $m_s = 0$ and $m_s = \pm 1$, which is therefore suppressed under normal conditions due to the dominant zero-field splitting. Yet, if the magnetic field is close to the ground state level anti-crossing (gs LAC), at $B_z \approx 1025$ G, this part of the Stark shift is not suppressed and it should be possible to measure the coupling constant R_{15} . A small additional transversal magnetic field has to be applied to enable the frequency shift. There are two competing mechanisms influencing the measurement. First, the electric field shift is suppressed by the magnetic field in axial direction in dependence on its distance from the gs LAC, and secondly the spin dependent fluorescence contrast becomes smaller the closer the magnetic field is to the gs LAC. So, a compromise has to be found for a magnetic field where there is still a significant R_{15} Stark shift and also sufficient ODMR contrast. We calculated that a $\Delta B_z = |B_{z,\text{LAC}} - B_z| = 2.3$ G and a transversal magnetic field $B_x \approx \Delta B_z$ leads to an expected shift about half ($0.97 E_{\perp} R_{15}$) of the maximum possible shift ($2 E_{\perp} R_{15}$) and still exhibits enough contrast for measurement. ODMR measurements for these magnetic field parameters are shown in fig. S6. The magnetic field was applied using two permanent magnets placed on actuator stages on either side of the diamond. As the transitions measured under these conditions are not protected from

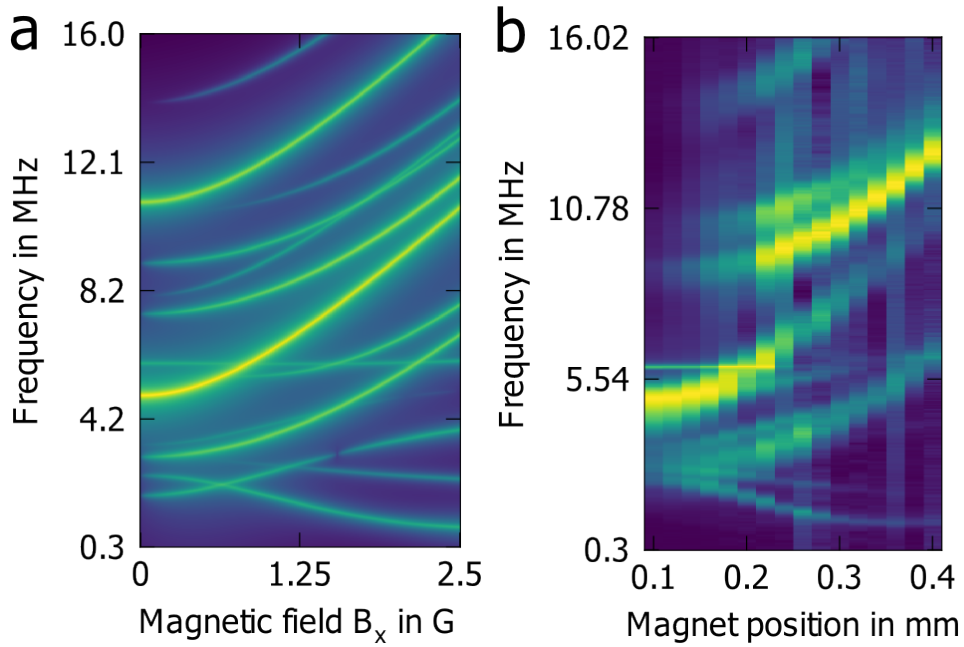


Figure S6: ODMR measurement at $B_z = B_{z,LAC} + 2.3$ G. (a) Simulation and (b) Measurement. Small differences arise from the unknown microwave polarisation, a not precise B_z field and a possible magnetic field change in transversal direction as the magnet position was changed using a micrometer stage where the axis is not perfectly aligned.

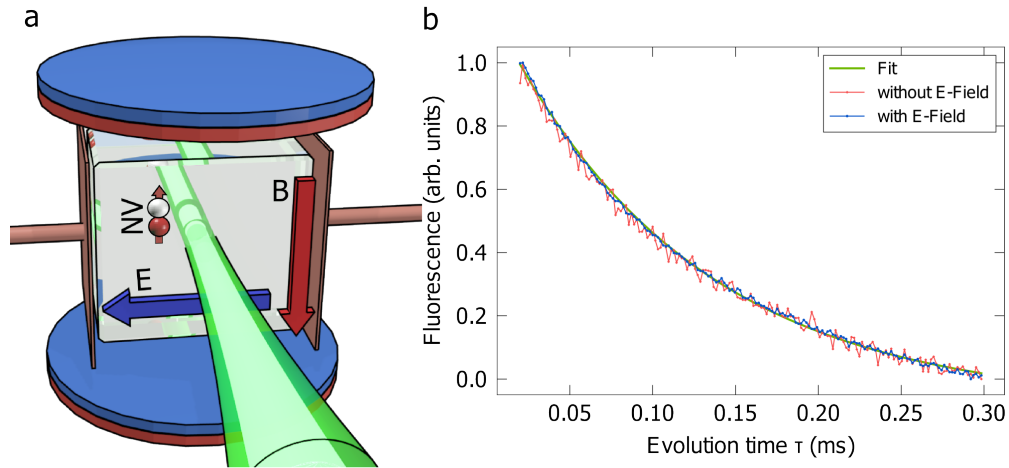


Figure S7: Measurement at the gs LAC. (a) Schematic of setup. Two permanent magnets are placed on stages on opposite sides of the diamond such that the magnetic field adds up to around 1025 G in 111-direction. The electric field is applied perpendicular to this magnetic field. (b) Hahn-Echo measurement with and without an applied magnetic field. With an applied electric field of 10 kHz, a dip should be visible at $\tau = 100 \mu\text{s}$.

magnetic field fluctuations, the coherence times are lower and thus we applied an electric field with 10 kHz. In a Hahn-Echo measurement, similar to the measurement presented in fig. 2 of the main text, no features of the applied electric field are visible, as can be seen in fig 7. Hence, the coupling constant R_{15} can not be measured, but an upper limit can be given. This limit is calculated as follows. The measured Hahn-Echo has a signal-to-noise ratio of $S/N \approx 62$. The phase Φ accumulated during a Hahn-Echo measurement with τ set for the highest sensitivity (so, for a 10 kHz signal to 100 μ s) has thus the upper limit with $S/N = 1$ of

$$1 - \cos \Phi \leq 1/62 \Rightarrow \Phi \leq 10.31^\circ. \quad (\text{S32})$$

The accumulated phase during a Hahn-Echo measurement is given by

$$\Phi = \frac{a}{f} (2 \cos(\pi f \tau) - \cos(2\pi f \tau) - 1), \quad (\text{S33})$$

where a is the amplitude of the frequency shift and f the signal frequency. This leads to the upper limit for a of

$$a \leq 0.45 \text{ kHz}. \quad (\text{S34})$$

The shift of the transition used is

$$\Delta f \approx 0.97 a R_{15}. \quad (\text{S35})$$

The amplitude of the shift a is known from the measurement at low magnetic fields for the other part of the Hamiltonian with R_{2E} . Here, the shift measured at the highest applied voltage was $a \approx 10$ kHz. Thus, the minimal measurable frequency shift is

$$\Delta f = 0.97 \cdot 10 \text{ kHz} \cdot \frac{R_{15}}{R_{2E}} \leq 0.45. \quad (\text{S36})$$

This means for the ratio of the coupling constants

$$\frac{R_{15}}{R_{2E}} \leq \frac{0.45}{0.97 \cdot 10} = 0.0464 \quad (\text{S37})$$

and therefore our measurement shows an upper limit for the R_{15} constant of

$$R_{15} \leq 0.0464 R_{2E} = 7.66 \text{ kHz}/(\text{V}/\mu\text{m}). \quad (\text{S38})$$

Data Analysis

Before the laser beam is directed onto the diamond, a part of the beam is splitted off and directed towards a second photo detector (both photodetectors are Thorlabs PDA100A) for reference of the laser power. The reference beam is dimmed as to match the detected fluorescence. Both photo detectors are read out simultaneously. The signal is divided by the reference to suppress the effect of laser power fluctuations. For the analysis, the thusly acquired signal over the duration of a laser pulse is divided into three equally long parts. The second part is discarded, while the first part is summed up and divided by the sum over the last part. This references out low frequency changes in the ratio of the measured light power between the two photo detectors. This results in a single value close to 1 for every pulse in a pulsed measurement sequence and which entails the spin state information.

Allan deviations

For the Allan deviations shown in Fig. 2(d) and Fig. 4(d) (here again shown in Fig. S8(c))(only green curve) of the main paper, a train of measurement sequences were conducted without an applied electric field. The measured noise could be recalculated into an electric field noise by separately measuring the signal over different applied electric field amplitudes.

For Fig. 2 d), this calculation is straight forward. The signal over the electric field amplitude forms a cosine as the cosine of the collected phase Φ_{acc} is measured. Here, the electric

field amplitude for which this measurement is most sensitive is at a voltage amplitude of about 4.8 V. We measured a train of Hahn-Echo measurements without applied electric field and from this, calculated the expected sensitivity by using the linear dependence between measurement signal and applied electric field at 4.8 V.

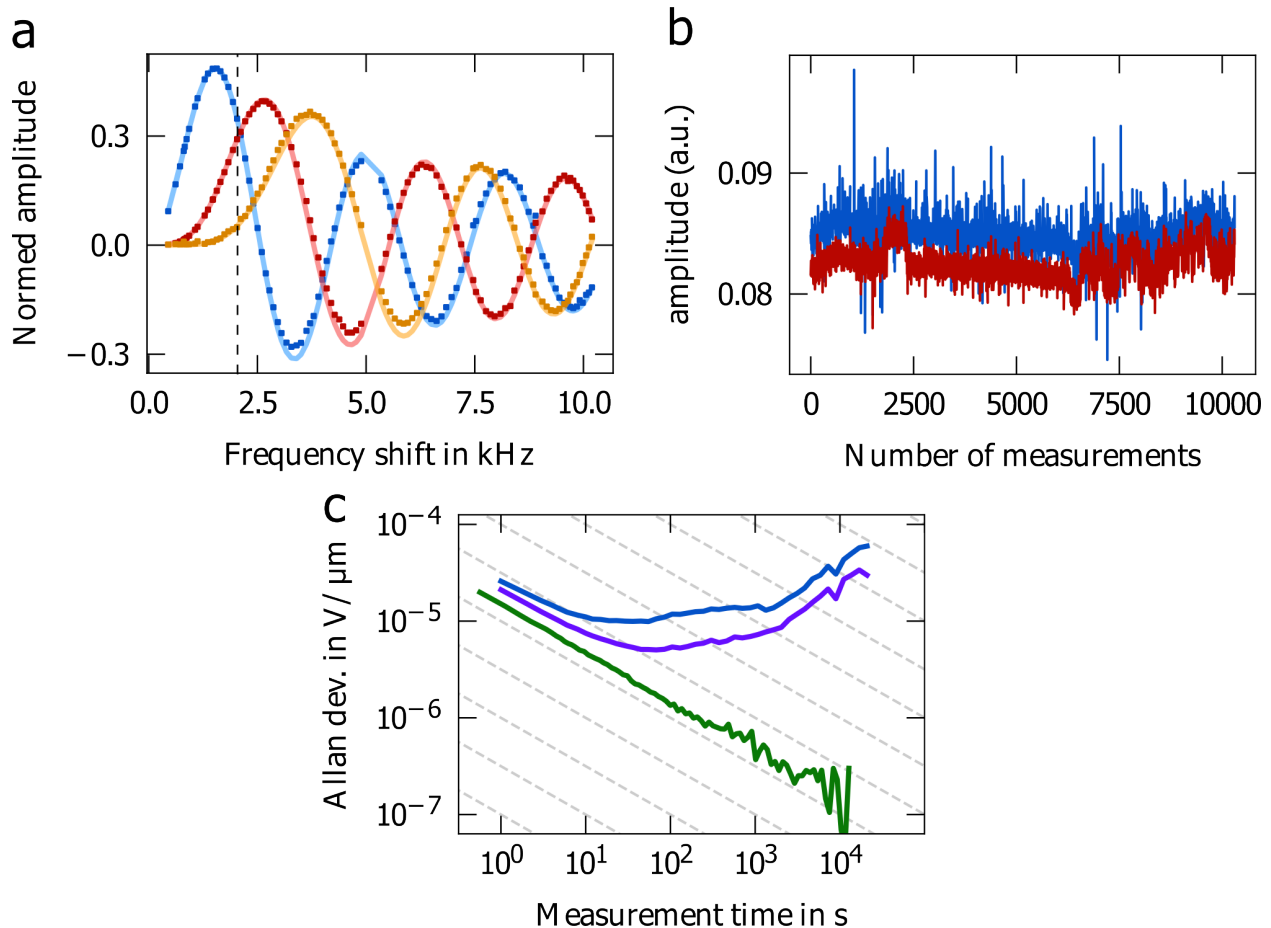


Figure S8: Calculation of Allan deviation shown in fig. 4 d) of the main paper. a) For this, a voltage amplitude is chosen where the Fourier components of $2f$ (blue) and $4f$ (red) are similar (dashed line). b) Fourier components over repeated measurements. The two components show a similar drift, which can be contributed to changes in the contrast, either due to a change in the transition frequency caused by magnetic field or temperature shifts or due to fluctuations in the laser power, which are not completely cancelled out by the referencing described above. c) Resulting Allan deviation for the sensitivity calculated using only one Fourier component (blue), the ratio between two Fourier components (purple) and the sensitivity without an applied electric field signal.

For the blue and purple lines in Fig. 4 d), we chose to perform the measurement at a voltage amplitude of about 6.7 V, corresponding to a maximum frequency shift for the

NV spin transition of 2.1 kHz and indicated by the dashed line in fig. S8(a). At that point, the Fourier component at $2f$ and at $4f$ are similar and both change linearly over the voltage amplitude in first order. Thus, the noise in the $2f$ Fourier component can be recalculated into an electric field noise and the Allan deviation for this is given by the blue line. As can be seen in fig. S8(b), the Fourier components for $2f$ and $4f$ drift and jump over time simultaneously. This is not a change in the electric field, which would result in an opposite movement of the two components. Rather, this can be attributed to a change in the contrast of the measurement, as the components are proportional to the contrast. A change in contrast can arise by a change of the NV spin transition frequencies, either by a change in temperature or a change in magnetic field. To overcome the contrast shift, we calculate the sensitivity also by using the ratio between the $2f$ and $4f$ Fourier components. This ratio is independent of the contrast and also linear to the electric field amplitude in first order. The achieved sensitivity using this ratio is shown in fig. 4(d) of the main paper and fig. S8(c) here as the purple line. It can be seen, that this sensitivity scales slightly longer with $1/\sqrt{\text{Hz}}$ as the blue line, which uses only one component.

For the green line in fig. 4(d) (here fig. S8(c)), the same measurement as used for fig. 2(d) was evaluated, analogous to the evaluation of the purple line described above. For this, the averaged Fourier components at $2f$ and $4f$ of the measurement with an applied signal was added to the noise of the measurement without signal at those two frequencies.

Analysis of the Fourier components

For fig. 4(b) in the main paper, the measurement was conducted over a range of applied electric field amplitudes. For each measurement, the averaged Fourier components at multiples of $2f$ are calculated. Using the first 5 components, the maximum shift caused by the electric field, a , and the contrast are fitted for each measurement point. The measurement points are then normed using the fitted contrast, to account for shifts in the contrast over the different measurements. A plot entailing the first five components is shown in fig. S9.

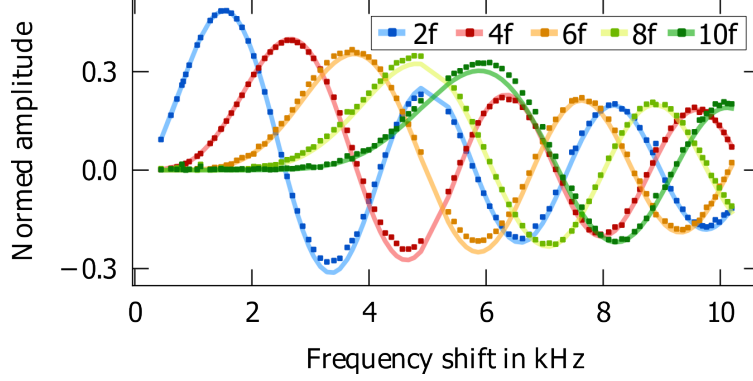


Figure S9: The first five Fourier components ($2f$ - $10f$) over the calculated frequency shift amplitude a .

Double Quantum Transition

For the measurements presented in fig. 2 and 4 of the main paper, the measurement was conducted with the electron spin being in a superposition state between $|0\rangle$ and the $|\pm\rangle$ states. These states are defined in eq. 5 and eq. 6 of the main paper. As those two states shift with opposite sign due to an electric field, a measurement utilizing the superposition between $|+\rangle$ and $|-\rangle$, leads to a phase evolution two times faster than the phase evolution of the single quantum transition. The scheme for a Hahn-Echo measurement with a double quantum transition is shown in fig. S10(a).

Pulse errors lead to a part of the population remaining in a superposition between $|0\rangle$ and $|\pm\rangle$. This part of the population collects half the phase during the free evolution time τ . We assume that the fidelity of the pulses does not change over the applied electric field strength. In fig. S11, the simulation is shown for different fractions of the population in the SQT. As the phase evolution is exactly double for the DQT compared to the SQT, this can be simulated by adding $(1 - c) \cdot s(t, 2a) + c \cdot s(t, a)$ (for $s(t)$ see eq. S18) with c being the fraction of the population in a superposition between $|0\rangle$ and $|\pm\rangle$ during the Hahn-Echo evolution time τ (SQT). Fig. S10(c) shows an Allan deviation measured at 6.4 kHz frequency shift amplitude. A comparison to the Allan deviations shown in fig. S8(c) shows, that the sensitivity is much lower. This may be attributed to a higher noise level due to the higher

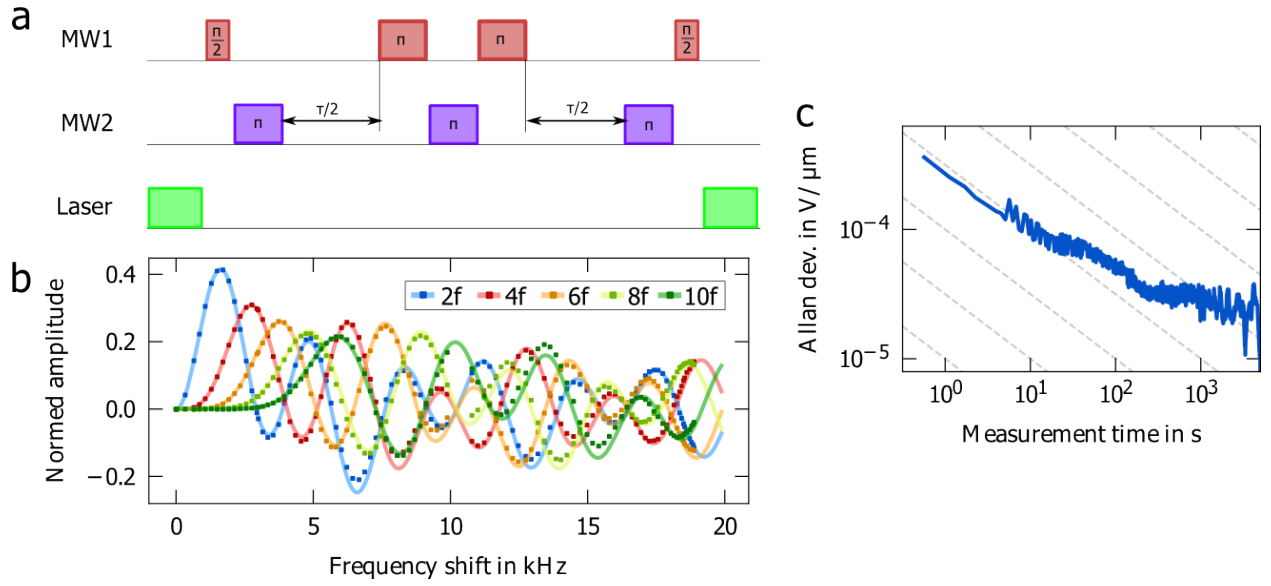


Figure S10: a) Double quantum transition measurement scheme. Two different microwave frequencies (MW1 for $|0\rangle \leftrightarrow |+\rangle$ and MW2 for $|0\rangle \leftrightarrow |-\rangle$) are employed to create a superposition state between $|+\rangle$ and $|-\rangle$. b) The five first Fourier components for a double quantum transition measurement over the amplitude of the frequency shift caused by the applied electric field on the single quantum transition. The phase collected during the free evolution time τ is doubled for the double quantum transition in relation to the single quantum transition. c) Allan deviation of this measurement using the first two Fourier components (blue and red in b)). The measurement was conducted with an electric field corresponding to a frequency shift amplitude of 6.4 kHz.

complexity of the measurement scheme.

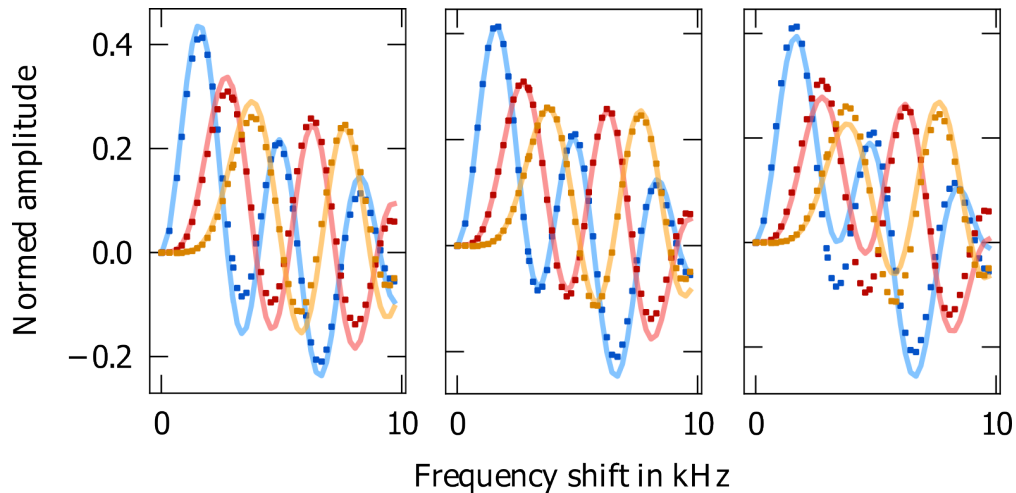


Figure S11: Effect of percentage of SQT in the DQT simulation. From left to right: 20%, 30% and 40% of the measured signal originates from a SQT. This percentage was assumed to be constant over the measurements.

References

- (S1) Doherty, M. W.; Michl, J.; Dolde, F.; Jakobi, I.; Neumann, P.; Manson, N. B.; Wrachtrup, J. Measuring the defect structure orientation of a single NV- centre in diamond. *New Journal of Physics* **2014**, *16*.
- (S2) Oort, E. V.; Glasbeek, M. Electric-Field-Induced Modulation of Spin Echoes of N-V Centers in Diamond. *Chemical Physics Letters* **1990**, *168*, 529–532.